Additive Manufacturing 66 (2023) 103467

Contents lists available at ScienceDirect

Additive Manufacturing

journal homepage: www.elsevier.com/locate/addma

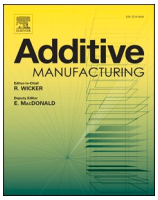

Laser powder bed fusion of Cu-Ti-Zr-Ni bulk metallic glasses in the Vit101 alloy system

Maximilian Frey [a,*], Jan Wegner [b], Erika Soares Barreto [c], Lucas Ruschel [a], Nico Neuber [a], Bastian Adam [a], Sascha Sebastian Riegler [a], Hao-Ran Jiang [d], Gerd Witt [b], Nils Ellendt [c], Volker Uhlenwinkel [c], Stefan Kleszczynski [b], Ralf Busch [a]

[a] Chair of Metallic Materials, Saarland University, Campus C6.3, 66123 Saarbrücken, Germany
[b] Chair of Manufacturing Technology, University Duisburg-Essen, Lotharstraße 1, 47057 Duisburg, Germany
[c] Leibniz Institute for Materials Engineering - IWT, Badgasteiner Str. 3, 28359 Bremen, Germany
[d] Materials Genome Institute, Shanghai University, Shanghai 200444, China

ARTICLE INFO

Keywords:
Bulk Metallic Glasses
Amorphous Metals
Additive Manufacturing
Laser Powder Bed Fusion
Mechanical Properties

ABSTRACT

Laser powder bed fusion (PBF-LB/M) of bulk metallic glasses (BMGs) has experienced growing scientific and industrial interest in the last years, with a special focus on application relevant systems based on zirconium. The high cooling rates and the layer-wise build-up process allow overcoming size and geometry limitations typical for conventional casting routes. Yet, the novel production approach requires different alloy characteristics than casting processes. The present work reports for the first time on the PBF-LB/M-processing of three CuTi-based bulk metallic glass formers in the Vit101 system, allowing to exceed the mechanical performance of most additively formed Zr-based BMGs. Furthermore, the influence of alloy properties like thermal stability and toughness on the PBF-LB/M applicability are systematically studied. Thermal stability plays a minor role to produce amorphous specimen, while notch toughness is found to be a more crucial aspect to achieve parts with low defect density and resulting high mechanical performance. The results suggest fundamentally different alloy development strategies adapted to the needs of the PBF-LB/M-process, leaving classical casting-based optimization of glass forming ability behind and evolving towards a rather toughness-oriented optimization.

1. Introduction

Bulk metallic glasses (BMGs) are a novel class of engineering materials. They combine the high strength and hardness of metals with elastic limits of up to 2 % usually only known from polymers, making them highly interesting materials for manifold industrial applications [1]. BMGs can be produced by rapid cooling of the equilibrium liquid to bypass crystallization and achieve vitrification at the glass transition temperature. The glass forming ability (GFA) of a given BMG-forming alloy can be quantified by its critical cooling rate (CCR), which defines the lowest cooling rate that allows suppressing crystallization to form a fully amorphous specimen. For conventional casting processes, the CCR imposes limitations in geometry and size, expressed by the critical diameter (d_c), which is the maximum diameter that permits full vitrification of a rod-shaped cast sample. Such limitations for conventional casting processes hinder the industrial application of BMGs until today.

Additive manufacturing (AM) through laser powder bed fusion (PBF-LB/M) of metals bears the potential to overcome the size and geometry constraints of casting processes. The layer-wise build-up principle with its small melt pool dimensions incorporates highly localized melting and solidification processes with extremely fast cooling rates of up to 10^6 K/s [2], which is far beyond the usual CCRs of modern BMGs, which range in the order of roughly 100 K/s. Studies have demonstrated the possibility to produce amorphous Fe-, Ti-, Cu-, and especially Zr-based metallic glasses [3–12] via PBF-LB/M. Complex geometries that are difficult or impossible to cast have been realized, e.g., scaffold structures [3], topology optimized structures [8], honeycomb structures for lightweight applications [13], or even compliant mechanisms [14]. Furthermore, additively formed BMGs can be post-processed by thermoplastic forming (TPF) [15], allowing to apply advanced surface finishing and structurization in a direct and efficient manner, unfeasible for crystalline

* Corresponding author.
E-mail address: maximilian.frey@uni-saarland.de (M. Frey).

https://doi.org/10.1016/j.addma.2023.103467
Received 29 October 2022; Received in revised form 23 February 2023; Accepted 23 February 2023
Available online 25 February 2023

metallic materials [16].

A major drawback of metallic glasses produced via PBF-LB/M is still found in their mechanics. Effects like porosity, (nano-)crystallization, structural relaxation, and chemical impurities usually lead to brittle fracture below the material's yield strength [17–20]. One of the few exceptions is found in the commercially available Zr-based system $Zr_{59.3}Cu_{28.8}Al_{10.4}Nb_{1.5}$ (trade name AMZ4 or Zr01 [21]) that has shown to reproducibly reach the alloy's yield strength of about 2.1 GPa for AM samples before failure in (macroscopic) bending tests [13,16,18]. Yet, the oxygen affinity of the Zr-based alloy together with the oxygen-triggered crystallization kinetics [22] necessitates rather high-purity powder feedstock to reach such high strengths combined with robust process stability [18]. Here, CuTi-based alloys like Vit101 ($Cu_{47}Ti_{34}Zr_{11}Ni_8$) [23] might emerge as a promising alternative, as they feature low material costs, increased strength, and smaller sensitivity to oxygen compared to most Zr-based alloys [24]. G. Garrett et al. [25] showed that microalloying of Vit101 with Si ($Cu_{47}Ti_{33}Zr_{11}Ni_8Si_1$ [26], further termed Vit101Si) and a combination of Si and Sn ($Cu_{47}Ti_{33}Zr_{11}Ni_6Si_1Sn_2$ [27], further termed Vit101SiSn) leads to three main effects. Firstly, the GFA increases from a critical diameter of 4 mm for Vit101 to 7.4 mm for Vit101Si and 6 mm for Vit101SiSn. Secondly, the width of the supercooled liquid (SCL) region increases, making Vit101Si and especially Vit101SiSn thermally more stable against crystallization in the low-temperature regime around the glass transition. Thirdly, the mechanical properties change in the way that the alloys become harder, yet increasingly brittle with an increasing degree of microalloying. Hence, alloying with Si and Si-Sn was found to be a double-edged sword in terms of industrial applicability. On the one hand, establishing a fully amorphous state through casting is facilitated through the increased GFA, also, TPF processability is improved through the enhanced thermal stability. On the other hand, the glassy state is found to be intrinsically more brittle, leaving produced parts less resilient against crack propagation and catastrophic failure. This ambivalent effect of microalloying also applies for PBF-LB/M processing: The higher thermal stability should toughen the material against crystallization caused by the process-typical cyclic remelting and annealing, but the increased brittleness could provoke crack formation and diminish the mechanical performance of manufactured parts.

Recently, Barreto et al. [28] have demonstrated that fully amorphous, PBF-LB/M-applicable powders of Vit101, Vit101Si, and Vit101SiSn can be atomized from commercial grade elements. The present work continues this research by evaluating the microalloying-induced trade-off between thermal stability and fracture toughness of these CuTi-based compositions during PBF-LB/M processing. In this matter, an PBF-LB/M parameter study was carried out to determine the processability in view of the fabrication of amorphous, dense, and mechanically resilient samples, heading towards a deeper understanding of specific requirements and challenges to adapt BMG compositions for AM.

2. Materials and methods

Fully amorphous powders of Vit101, Vit101Si, and Vit101SiSn with oxygen contents of 760 ± 22, 750 ± 10, and 737 ± 35 µg/g, respectively, and particle diameters between 20 and 63 µm were prepared by close-coupled gas-atomization (CCA) as described in [28]. Cuboid-shaped samples (2.5 × 5 × 5 mm^3, height × width × length) were additively manufactured under Argon gas atmosphere using an SLM 280 HL incorporating two 700 W fiber lasers with spot diameters of 70 µm. All samples were processed on top of preheated Ti6Al4V substrates at 373 K with a layer thickness d_s of 20 µm and a hatch distance h of 70 µm. The cuboid samples were produced for all three alloys with varying values of laser power and scan speed to define a range of parameters for fully amorphous samples with optimized relative density. The laser power P was changed in 10 W steps from 50 W to 80 W, which is taken into account in the sample notation by groups of samples being termed A (50 W), B (60 W), C (70 W), and D (80 W). Within these groups, the scan speed v_s was changed from 1600 mm/s to 2200 mm/s in 200 mm/s steps, indicated by the numbers 1–4. The volume energy density E_V of each sample can be calculated as

$$E_V = \frac{P}{v_s d_s h}. \quad (1)$$

Table 1 summarizes laser powers, scan speeds and the resulting volume energy densities for all samples, which range between 16.2 and 35.7 J/mm^3. Besides the cuboid samples, beam-shaped samples for mechanical testing (1.9 × 2.8 × 25.2 mm^3) were built using the medium-energy parameter set C3 (70 W, 2000 mm/s, 25.0 J/mm^3) and the high-energy parameter set D1 (80 W, 1600 mm/s, 35.7 J/mm^3). The reason for choosing these parameters will be justified later.

Cuboid samples were mechanically removed from the substrate for further analysis. Sample preparation consisted of wet cutting the cuboids in half along the build direction and hot embedding one half in epoxy resin (Technotherm 3000). The microsections were then sanded and polished to analyze the relative optical density via light microscopy using an Olympus BX51M device. Complementary, porosity and microstructure of two polished Vit101Si microsections formed with the low-energy parameter set A3 (50 W, 2000 mm/s, 17.9 J/mm^3) and the high-energy parameter set D2 (80 W, 1800 mm/s, 31.7 J/mm^3) were studied via a Zeiss Sigma VP scanning electron microscope (SEM) in secondary electron (SE) imaging mode and back-scattered electron (BSE) imaging mode.

The remaining cuboid halves were analyzed in terms of their structural and thermophysical properties using X-ray diffraction (XRD) and differential scanning calorimetry (DSC). Both methods investigate a relatively large sample region or volume, and therefore provide averaged information over a large number of additively formed layers. XRD-measurements on the sanded center area of the cuboid halves were carried out with a Bruker D8-A25 diffractometer applying the K_α-radiation of Cu with a wavelength of 1.5406 Å. For calorimetry, the cuboid halves were again cut along the build direction to achieve samples with masses in the order of 25 mg. DSC temperature scans were performed with a Perkin-Elmer DSC8000 under high-purity Ar flow in copper crucibles. The samples were heated from 323 K to 973 K with a heating rate of 1 K/s.

High-energy synchrotron X-ray diffraction (HESXRD) was performed on the samples with the highest volume energy density (D1) to clarify if small crystalline fractions are present, that cannot be resolved with conventional laboratory-scale methods. The room temperature measurements in transmission mode were performed at P21.2 beamline facility of PETRA III of the Deutsche Elektronen-Synchrotron (DESY). Radiation with a wavelength of 0.177138 Å (70 keV) was used, the beam size was 500 × 500 $µm^2$. The setup featured a sample detector distance of 949 mm and was geometrically calibrated via the diffraction

Table 1
Process parameters and resulting volume energy densities of the PBF-LB/M-formed cuboid samples. Each combination of scan speed and laser power leads to a specific volume energy density, which is given in the respective cell of the table. The corresponding sample notation is added in the right lower corner of each cell.

Volume energy density (J/mm^3) *(Sample notation)*		Laser power P (W)			
		50 *(A)*	60 *(B)*	70 *(C)*	80 *(D)*
Scan speed (mm/s)	1600 *(1)*	22.3 *(A1)*	26.8 *(B1)*	31.3 *(C1)*	35.7 *(D1)*
	1800 *(2)*	19.8 *(A2)*	23.8 *(B2)*	27.8 *(C2)*	31.7 *(D2)*
	2000 *(3)*	17.9 *(A3)*	21.4 *(B3)*	25.0 *(C3)*	28.6 *(D3)*
	2200 *(4)*	16.2 *(A4)*	19.5 *(B4)*	22.7 *(C4)*	26.0 *(D4)*

pattern of CeO_2. A VAREX XRD4343CT detector (2880 × 2880 pixels) recorded the two-dimensional dark-image-corrected diffraction pattern that was recorded with an acquisition time of 5 s per sample. The pattern was further integrated using PyFAI and then processed with the PDFgetX2 software [29] to obtain the background-corrected scattering intensity I(Q). Furthermore, the two-dimensional pattern were also caked in 8 pieces with an azimuthal range of 45° to check for crystalline reflexes with a further improved signal-to-noise ratio.

Macroscopic mechanical testing of the beam samples was performed in a three-point-beam bending (3PBB) setup with a Shimadzu testing machine as described in detail in [13]. Due to the large interface area between sample and substrate, the beams were removed by electric discharge machining (EDM). The surface of the beams was sanded (1200 grid) to exclude the influence of surface roughness acting as crack initiation sites [30] and to achieve a well-defined geometry. Four to five specimens per alloy and parameter set allowed for statistics. The engineering stress σ and strain ε on the specimen surface are calculated as

$$\sigma = \frac{3FL}{2bh^2} \tag{2}$$

and

$$\varepsilon = \frac{6Dh}{L^2}. \tag{3}$$

Here, F is the applied force, L is the support span of 20 mm, b is the sample width, h is the sample height, and D is the displacement at the sample center. Complementary, the morphology of fracture surfaces was further analyzed via SEM imaging (SE) as described above.

Besides the AM samples, as-cast beam-shaped samples in the same geometry as the additively manufactured beams were produced to serve as references for DSC and mechanical analysis. In a first step, high-purity raw elements were arc-melted and mixed under a Ti-gettered high-purity Argon atmosphere on a water-cooled copper plate. Several remelting steps ensure the formation of a homogeneous yet still crystalline master alloy. In a second step, the material was remelted by arc-melting and subsequently suction cast in a water-cooled copper mold to form a completely amorphous beam. A detailed description can be found in e. g. [31,32].

The oxygen contents of AM beam-shaped samples manufactured with the parameter set D1 as well as the as-cast beam references were measured via hot gas carrier extraction (ELTRA ONH-2000) using helium (99.999 %). Five specimens per sample were measured and the results were averaged.

3. Results

3.1. Light microscopy

In a first step to assess the applicability of the three alloys for the PBF-LB/M process, the process stability and crack formation in the cuboid samples are qualitatively evaluated. As often described by literature [10,18], lack of fusion (LOF) defects decrease with increased volume energy density (at least for moderately high energy densities as investigated in this study), as clearly visible in Figure A in the Supplementary Material. This tendency will be later quantified by optical density results in subsection 3.2. Furthermore, a clear trend is observable as process-induced cracking and porosity are promoted by an increasing number of microalloying components. In Fig. 1, representative light microscopy images of the D1 samples with the highest volume energy density (35.7 J/mm^3) of all three alloys are compared. Vertical cracks are visible in the Vit101 and Vit101Si microsections. The cracks initiated from the base of the samples previously in contact with the build platform, which is known to be a weak spot region in PBF-LB/M processing of BMGs [33]. This is likely to be caused by the dissimilar pairing of the CuTi-based BMGs and the Ti6Al4V substrate plate. The mismatch of the thermal expansion coefficients induces thermal stresses. Additionally, the intermixing of the alloys may lead to the weakening of the interface region due to the formation of intermetallic phases [34,35]. Nonetheless, the bulk material seems to withstand the apparent residual stresses during the consecutive build-up. On the contrary, Vit101SiSn reveals horizontal and vertical cracks in the prepared cross-sections. Horizontal cracks are initiated by in-plane residual stresses that originate from the rapid solidification. The thermal gradients between the exposed and the solidified layer typically induce large tension stresses during cooling, which mostly dominate the residual stresses in PBF-LB/M [36–38]. Apparently, the residual stresses exceed the strength of the PBF-LB/M processed Vit101SiSn which leads to the observed cracking in the bulk sample volume. Yet, Vit101 and Vit101Si withstand the in-plane stresses for the given conditions. The crack formation applies to the majority of Vit101SiSn samples, resulting in numerous losses of samples through harshly ruptured cuboids. Eventually, sample fragments interfered with the powder deposition and led to increased LOF.

As no meaningful set of specimens could be obtained, Vit101SiSn was excluded from further analysis. Besides these composition-specific effects, it is found for all three alloys that samples manufactured with the highest scan speed of 2200 mm/s (parameter set “4”) tend to feature an unstable sample-substrate connection. This results in relatively frequent sample losses during processing. Accordingly, the lost samples are also not part of further analysis.

3.2. Diffraction, calorimetry, and density studies

Figs. 2(a) and (b) display all XRD results of the Vit101 and Vit101Si cuboid samples. The different colors indicate the laser power used to manufacture the respective specimen. For all investigated samples, the broad diffraction halo typical for amorphous materials together with the absence of crystalline reflexes can be observed. For e.g., an PBF-LB/M-formed Zr-based BMG (AMZ4), it has been demonstrated that a too high laser energy input can lead to thermally induced crystallization [10,18]. As small (nano-)crystalline fractions can be easily overlooked by conventional XRD due to the method’s resolution limits [16,39], the samples with the highest E_V value of 35.7 J/mm^3 (D1) are double-checked via HESXRD. This method allows the detection of smaller crystalline fractions due to the extremely brilliant synchrotron

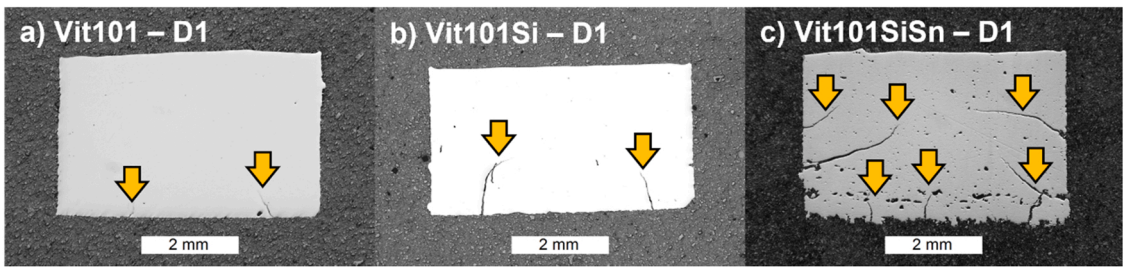

Fig. 1. Representative light microscopy images of the cuboid samples of all three compositions produced with the highest volume energy density of 35.7 J/mm^3 (D1). The build direction is from the bottom towards the top. With growing degree of microalloying, the tendency to form defects like pores and cracks increases.

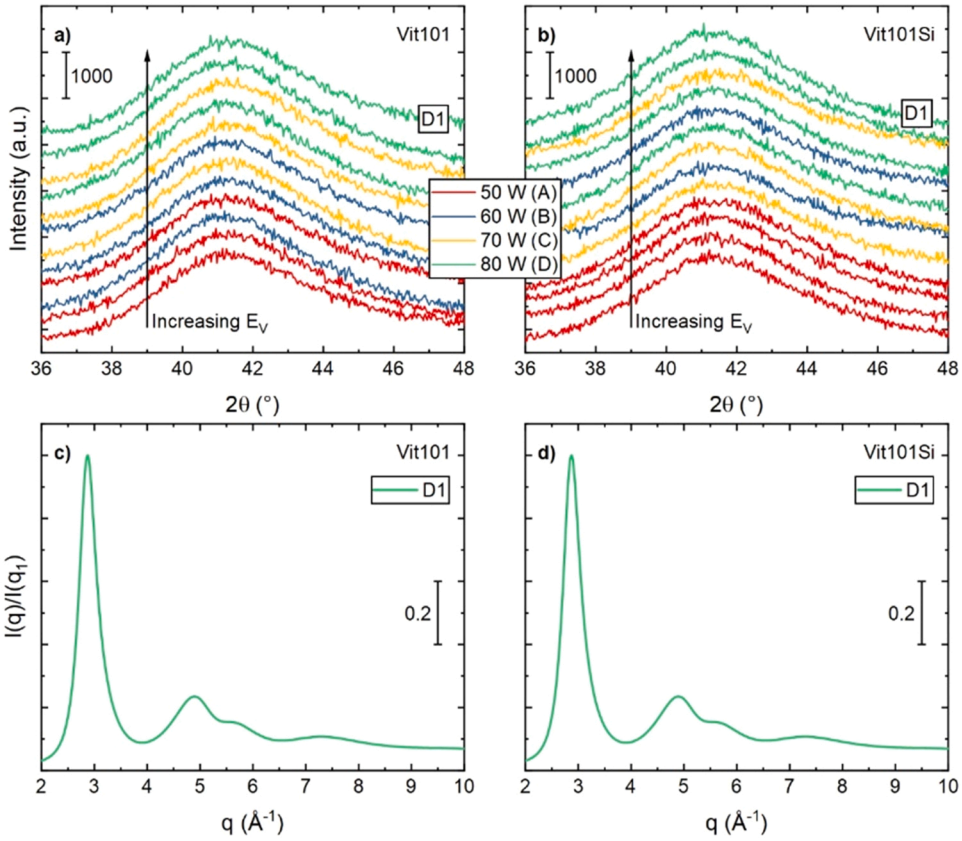

Fig. 2. In (a) and (b), all XRD diffractograms of the Vit101 and Vit101Si cuboid samples formed with different parameter sets are given. The applied E_V increases from the bottom to the top, the different colors indicate the applied laser power. No crystalline reflexes can be observed. The samples with the highest E_V (D1) are furthermore analyzed via HESXRD, the normalized background-corrected scattering intensities are given in (c) and (d). Again, crystalline reflexes are completely absent.

source and the resulting exceptional signal-to-noise ratio. Figs. 2(c) and 2(d) show the normalized background-corrected scattering intensity I(q)/I(q_1) of the D1 cuboids, which lack any crystal reflexes, thereby underlining the synchrotron-amorphous state of these samples. Also, the caking approach does not reveal reflexes, see Figure C in the Supplementary material. Hence, thermally induced crystallization effects can be mostly excluded for Vit101 and Vit101Si samples manufactured in the parameter range investigated in this work.

As reported in [28], the powder feedstock features 760 and 750 µg/g oxygen for Vit101 and Vit101Si, respectively. In the present work, the samples additively manufactured from this powder material with parameter set D1 (35.7 J/mm^3) show values of 857 ± 14 and 883 ± 16 µg/g oxygen contamination. In contrast, the high-purity as-cast samples only feature 168 ± 5 and 173 ± 7 µg/g oxygen for Vit101 and Vit101Si.

Complementary to the oxygen measurements, Figs. 3(a) and (b) display the DSC traces of the Vit101 and Vit101Si powder feedstock material (previously published in [28]), the D1 AM-samples as well as the as-cast references. For all Vit101 samples, the onset of the glass transition, T_g, occurs at about 690 K, followed by a short supercooled liquid (SCL) region of about 60 K length that is terminated by the onset of crystallization T_x at roughly 750 K. In contrast, the Vit101Si samples feature a 10 K longer SCL with a T_g of about 705 K and a T_x of roughly 775 K, confirming the previously reported increased thermal stability due to the Si addition [25,26,28]. For both alloys, neither the length of the SCL (i.e., the thermal stability) nor the shape, size, or position of the crystallization peaks appears to be strongly affected by the processing route and resulting oxygen content of the different DSC samples. The enthalpies of crystallization ΔH_x of all analyzed samples are determined by integration over the crystallization signal. Figs. 3(c) and 3(d) show ΔH_x for each AM cuboid as a function of E_V. Samples manufactured with the same laser power feature the same color. The ΔH_x values of the high-purity as-cast samples are found to be − 6980 J/g-atom for Vit101 and − 6810 J/g-atom for Vit101Si, exhibiting typical values for fully amorphous samples of the present compositions [27,40]. These values serve as reference marks for the AM samples and are indicated as dashed lines. For both alloys, the reference ΔH_x values are quite well reproduced by the high-laser-power parameter sets (“C” with 70 W and “D” with 80 W) with volume energy densities above roughly 25 J/mm^3. Samples with lower E_V (especially parameter sets “A” and “B”) tend to show deviations in form of less intense crystallization events with ΔH_x values of up to − 6000 J/g-atom.

In Figs. 3(e) and 3(f), the relative optical densities as a function of E_V are shown. Low E_V values lead to insufficient densification due to LOF and resulting porosity, especially for the low-laser-power parameter set “A” (50 W). LOF typically originates from an insufficient overlap of adjacent weld tracks, and thus, incomplete melting of the powder layer. The size of the melt pools correlates with the applied laser energy. Since multiple parameters (e.g., laser power, scan speed, or hatch spacing) affect the energy input, the volume energy density is often used as a measure for different parameter settings [41]. With rising E_V, densification improves towards a relatively stable plateau with more than 99 % densification for volume energy densities above roughly 25 J/mm^3. Hereafter, the density only slightly increases with further rise of E_V. For both alloys, the highest densification is achieved with the highest E_V of 35.7 J/mm^3 (D1), with 99.92 ± 0.03 % for Vit101 and 99.87 ± 0.09 % for Vit101Si. Figure A in the Supplementary material exemplarily demonstrates the trend from LOF-porosity to high-density with increasing E_V.

3.3. Scanning electron microscopy

Sample densification is further studied via SEM imaging of representative Vit101Si cuboids formed with the low-energy parameter set A3 and the high-energy parameter set D2, both highlighted in gray in Fig. 3(f). The A3 sample features a low optical density of 88.72 ± 1.15 %,

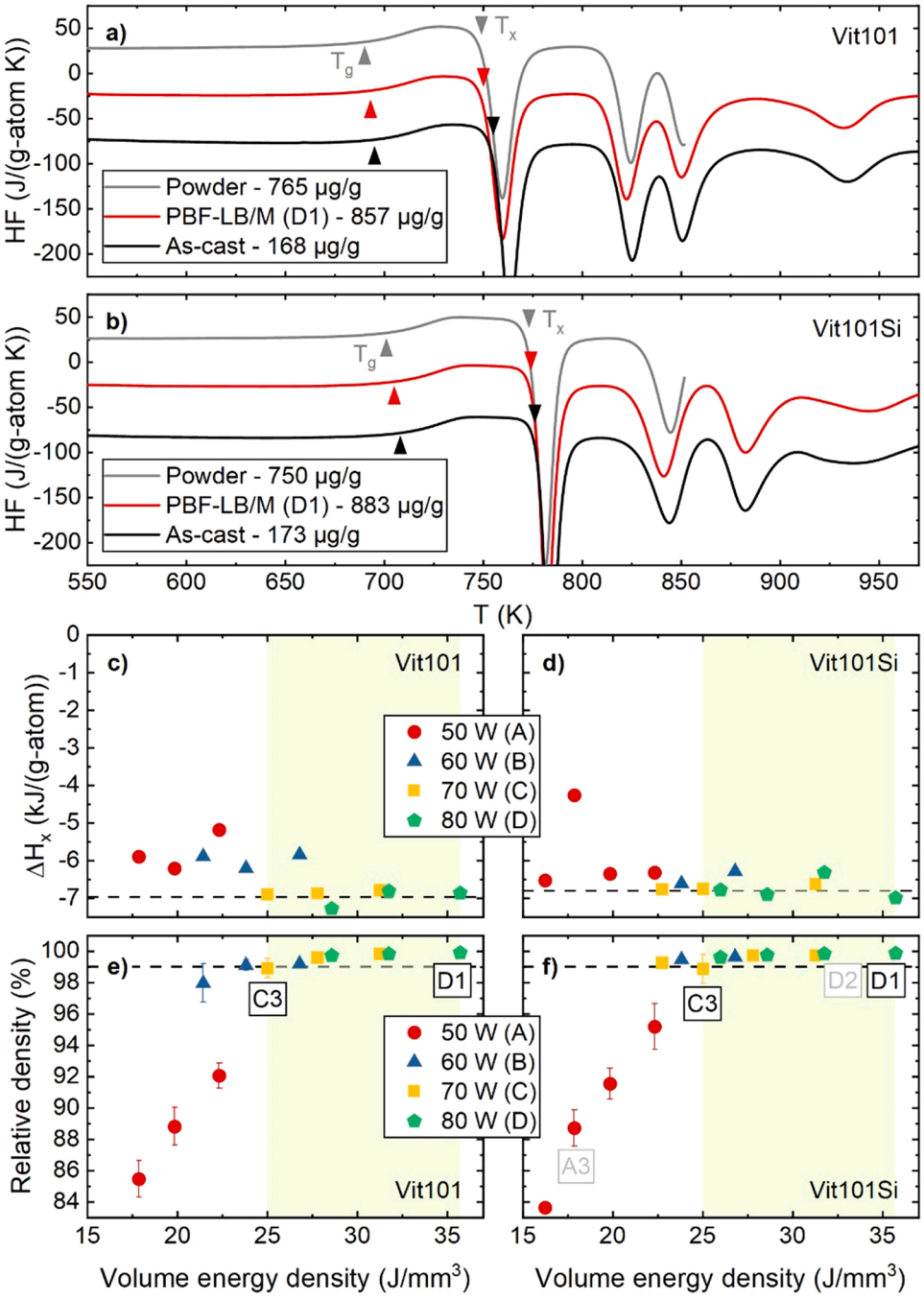

Fig. 3. In (a) and (b), DSC scans of powder material, representative samples PBF-LB/M-formed with the parameter set D1, and high-purity as-cast samples are shown for Vit101 and Vit101Si. The oxygen content of the samples is given in the captions. The powder DSC scans are taken from [28]. The crystallization enthalpy of all cuboid samples is determined by integration and displayed in (c) and (d) as a function of the applied volume energy density. Above about 25 J/mm^3, ΔH_x stabilizes at the level of the as-cast references (dashed lines). In (e) and (f), the respective relative optical densities are given, also as a function of the applied volume energy density (the error bars reflect the standard deviation). Low E_V results in insufficient densification, but above 25 J/mm^3, densities higher than about 99 % (dashed line) are reached. Hence, the optimized parameter window lies between the parameter sets C3 and D1 (highlighted), corresponding to an E_V range from 25 J/mm^3 to 35.7 J/mm^3, as indicated by the light green background. The cuboid samples A3 and D2 further analyzed by SEM imaging are highlighted in gray.

which is directly reflected by the SE image in Fig. 4a), where a large degree of porosity can be identified. Figs. 4(b) and 4(c) show higher-magnification SE and BSE images of representative pores, as indicated by the white frame in Fig. 4(a). These are irregular in shape and incorporate unmolten or only partially molten particles typical for LOF defects. The defects feature a slightly horizontal orientation, reflecting the layer-wise build process. Yet, no signs of crystallization in the form of a phase-contrast can be detected in the BSE image. In contrast, Fig. 4 (d) shows the SE image of the D2 sample that features a high optical density of 99.85 ± 0.01 %. Besides a distinct crack that originates from the sample-substrate interface, only sporadic pores can be identified, which show spherical geometry typical for gas enclosures.

3.4. Mechanical testing and fractography

Fig. 5 presents the three-point beam bending results. In Fig. 5(a), the as-cast specimen of Vit101 is depicted as black solid curves with a Young's modulus of 103.7 GPa and yield strength in the order of 2.5 GPa. A maximum strength of 3.30 GPa and a significant plastic regime of more than 3 % are observed. In the case of the high-energy parameter set D1, the additively formed Vit101 samples reach a Young's modulus of 100.1 ± 2.0 GPa and a maximum strength of 2.47 ± 0.05 GPa, while lacking significant plastic deformation. Contrastingly, the Vit101 samples formed with the medium-energy parameter set C3 show a distinctly lower Young's modulus of 85.8 ± 3.1 GPa, coupled with a relatively low maximum strength of 1.72 ± 0.17 GPa on average. Remarkably, the C3 samples show a higher scatter than the D1 samples, especially in terms of maximum strength. The as-cast Vit101Si sample in

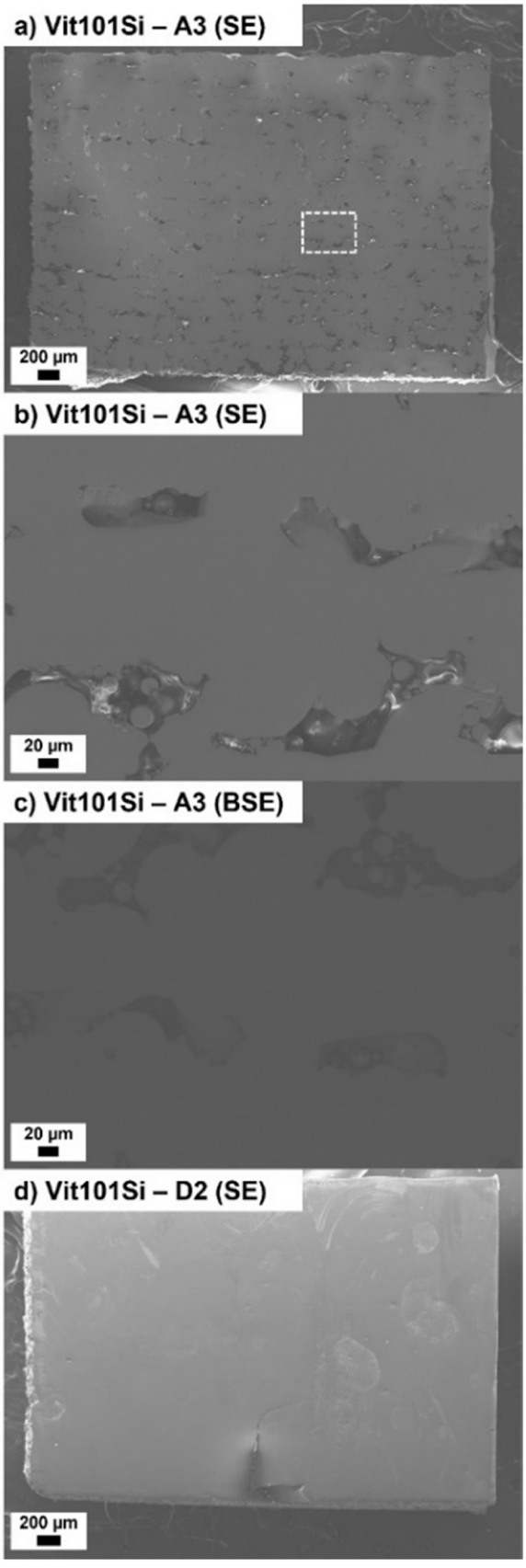

(caption on next column)

Fig. 4. SEM imaging of two representative cuboid samples. The build direction is always from the bottom towards the top. In (a), the low-energy sample A3 with a relative optical density of 88.72 ± 1.15 % is fully displayed via SE imaging. The irregularly shaped LOF-porosity is clearly visible. The region in the white rectangle is zoomed in in (b), where non-molten powder particles inside the pores can be recognized. (c) shows the same region imaged via BSE, no phase-contrast occurs. In contrast, (d) depicts the SE image of the D2 high-energy sample with a relative optical density of 99.85 ± 0.01 %. Besides a crack in the lower part, only sporadic and rounded gas pores are visible.

Fig. 5(b) behaves almost identically to the as-cast Vit101 sample, only with a reduced plastic deformation regime of about 1.5 %. Vit101Si samples additively formed with both parameter sets show a similar behavior as the Vit101 C3 samples: A noticeably decreased Young's modulus paired with a scatter-afflicted maximum strength below the reference's yield strength.

Fig. 6 provides SEM images (SE) of the fracture surfaces of Vit101 and Vit101Si D1 beams after 3PBB testing. Both fractograms in Figs. 6(a) and 6(b) show a similar appearance. A rather smooth and straight region is formed at the top of the samples (the region that experiences the highest tension stress, as the samples are loaded from below), which is often addressed to shear band forming and delamination [42]. The remaining majority of the fracture surfaces feature a rough appearance, typical for rapid fracture [42]. In this rough rapid fracture region, river-like structures can be observed, as shown in Figs. 6(c) and 6(d). Within these, typical dimple patterns are present, as shown in the zoomed-in regions in Figs. 6(e) and 6(f). For Vit101, homogeneous river structures with relatively pronounced and large-scale dimples are visible. In contrast, Vit101Si features rather heterogenous river structures, with less evolved dimples that show smaller scales than the ones observed for Vit101.

4. Discussion

4.1. Oxygen influence

The oxygen contamination of the present PBF-LB/M-formed specimens is roughly five times higher in comparison to the as-cast reference specimens. The reason can be found in the processing route itself: the AM samples are made from powder feedstock of industrial-grade purity with a high surface-to-volume ratio, which allows for a large oxygen absorption. Reviewing oxygen contaminations in comparable systems, Wang et al. [7] reported on PBF-LB/M-manufacturing of Ti-based metallic glass ($Ti_{47}Cu_{38}Zr_{7.5}Fe_{2.5}Sn_2Si_1Ag_2$) with 1250 µg/g oxygen content made from powder feedstock with 930 µg/g oxygen. PBF-LB/M-formed $Zr_{52.5}Cu_{17.9}Ni_{14.6}Al_{10}Ti_5$ metallic glass was reported to feature 920 µg/g oxygen, while the used powder includes 487 µg/g oxygen [43]. In the case of the commercially available $Zr_{59.4}Cu_{28.8}Al_{10.4}Nb_{1.5}$ (AMZ4), oxygen contents of powder feedstock can vary over a broad range from about 600 up to 2292 µg/g [18]. The comparability of these values might be limited due to various factors like the purity of the initially used raw elements, the choice of the powder atomization process, the respective process atmosphere, or also the particle fraction used, as smaller powder particles feature a larger surface-to-volume ratio and therefore a higher oxygen uptake [28]. Still, it can be claimed that the present CuTi-based alloy powders and AM-samples feature relatively moderate oxygen contaminations of about 750 and 850 µg/g, respectively, although the large content of Ti and Zr (together about 45 at%) would predetermine a strong oxygen affinity.

For Zr-based BMGs, it is well known that oxygen alters the crystallization mechanism by changing the primary phase and therefore decreases the GFA and thermal stability [21,44–47], and accordingly the robustness against thermally induced crystallization during PBF-LB/M processing [18,22]. In contrast, the GFA of Vit101 and its derivatives is reported to be relatively resistant against its deterioration through

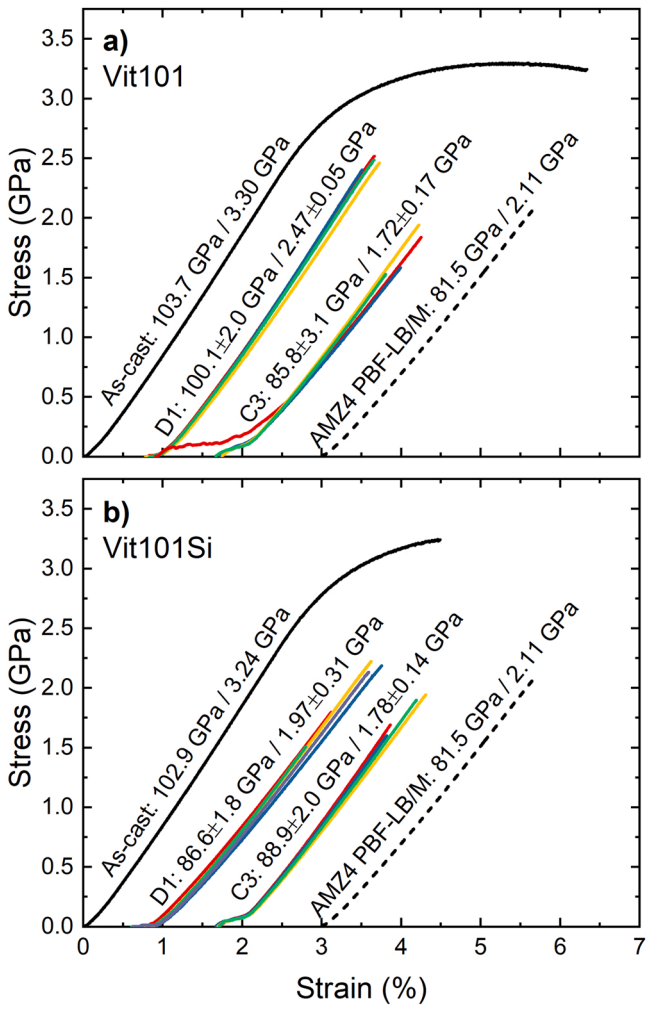

Fig. 5. Stress-strain curves determined by 3PBB mechanical testing for (a) Vit101 and (b) Vit101Si. The first value written on the curves reflects the Young's modulus, the second gives the maximum strength. The provided error values reflect the standard deviations. The as-cast curves are shown in black and serve as references. For comparison, the curves of PBF-LB/M-formed AMZ4, a Zr-based metallic glass former, are taken from [16,18] and added as black dashed lines. Only the D1 parameter sample set of Vit101 allows reaching the as-cast Young's modulus as well as its yield strength of about 2.5 GPa before brittle fracture occurs. All other parameter sets lead to a decreased Young's modulus as well as brittle fracture before the materials yield strength is reached. For some curves, the testing device causes artifacts in the low-strain regions, which are excluded for defining the Young's modulus.

impurities and especially oxygen contaminations, as no difference in critical casting diameter was found for samples cast from high-purity and industrial-grade material [24]. The presented DSC scans reveal that the length of the SCL, crystallization event morphology, and crystallization enthalpies of Vit101 and Vit101Si are practically unaffected by processing route and oxygen content, rendering the alloy system as a robust and well-suited candidate for the rather contamination-affected PBF-LB/M process.

4.2. PBF-LB/M parameter evaluation and microstructural aspects

While the XRD results in Fig. 2 suggest complete vitrification within the investigated parameter range, the ΔH_x values of low-energy samples built with low laser power (50 W and 60 W) and an E_V of less than roughly 25 J/mm^3 are distinctly higher (indicating a less intense crystallization event) than the fully amorphous reference, suggesting a partially crystalline structure, see Fig. 3. In the same E_V range below 25 J/mm^3, the optical density measurements reveal insufficient densification of less than 99 %. Both effects, the decreased crystallization enthalpy and the insufficient densification, might be linked in the way that cracks and high LOF-porosity could promote heat accumulations caused by decreased thermal dissipation, leading to localized crystallization effects. The cuboid samples further investigated via SEM imaging in Fig. 4 were chosen accordingly to verify this hypothesis. The high-energy parameter set D2 serves as a highly dense and fully amorphous (in terms of XRD and DSC) reference, while the low-energy A3 sample shows substantially lower density and the lowest measured crystallization enthalpy. The SE images in Figs. 4(a) and 4(b) allow to clearly characterize the LOF-porosity of the A3 sample, yet, signs of crystallization cannot be identified due to the lack of phase contrast, as shown by the representative BSE image in Fig. 4(c).

Glade et al. [48] have studied the isothermal crystallization behavior above T_g of Vit101. It was shown that phase separation and subsequent crystallization results in nanocrystals of only several nm in size. Bochtler suggested that the primary crystallization species of Vit101 upon heating and cooling is probably a $ZrTiCu_2$ laves phase, which features a marginal structural fingerprint even when analyzed with the excellent signal-to-noise ratio of HESXRD, as demonstrated by B. Bochtler in [24]. Hence, the small crystal size as well as the rather marginal diffraction signal of the primary crystallization phase seem to leave conventional SEM and XRD as unpreferable methods with too low resolution to identify partial crystallization in the present alloys. ΔH_x screening via DSC scans appears to be a more sensitive approach to resolve small nanocrystallization effects, as previously reported in [16]. Interestingly, the Zr-based AMZ4 does not show a comparable loss of ΔH_x when low E_V values create insufficient density and LOF, as exemplarily shown by Wegner et al. [18]. Therefore, the observed decrease in ΔH_x for low-E_V samples due to possible nanocrystallization might be an alloy-specific effect, which shall be investigated separately via high-resolution methods like TEM or broader use of HESXRD studies.

Besides such instabilities in the low-density parameter range below about 25 J/mm^3, XRD, DSC, and HESXRD show no signs of crystallization for Vit101 as well as Vit101Si, even for the highest E_V of 35.7 J/mm^3. This is a partially astonishing result, as Vit101Si features a significantly more stable SCL region in DSC scans than Vit101 with its only marginal SCL stability. Theoretically, the difference in thermal stability should result in a distinct advantage of Vit101Si in terms of robustness against higher E_V values, since it renders the alloy more resilient against the process-inherent cyclic thermal loads in the heat-affected zone of the melt pool. Yet, within the present parameter window, no differences can be identified, postponing the definition of the limiting E_V thresholds for retaining fully amorphous specimens to a successive study with larger laser intensities applied.

4.3. Mechanical performance

Summing up, an E_V range for the PBF-LB/M processing of highly dense and fully amorphous samples can be defined between about 25 and at least 35.7 J/mm^3, indicated by a light-green background in Figs. 3(c) – 3(f). The lower and upper boundaries of this process window are marked by the parameter sets C3 (2000 mm/s, 70 W) and D1 (1600 mm/s, 80 W), respectively. Previous studies on the Zr-based AMZ4 [16,18] showed that fully amorphous and density-optimized PBF-LB/M samples can reach the alloy's yield strength before brittle fracture without observable (macroscopic) plasticity occurs. Accordingly, the process window defining parameters C3 and D1 were chosen to build samples for the three-point bending tests.

The results in Fig. 5 reveal that only Vit101 manufactured with the high-energy parameter set D1 reaches the Young's modulus and the yield strength of the as-cast reference with an exceptional maximum strength of about 2.5 GPa. To our knowledge, this sets a new record for additively formed BMGs measured in (macroscopic) beam bending, outperforming the previous record-holder AMZ4 [16,18] by about

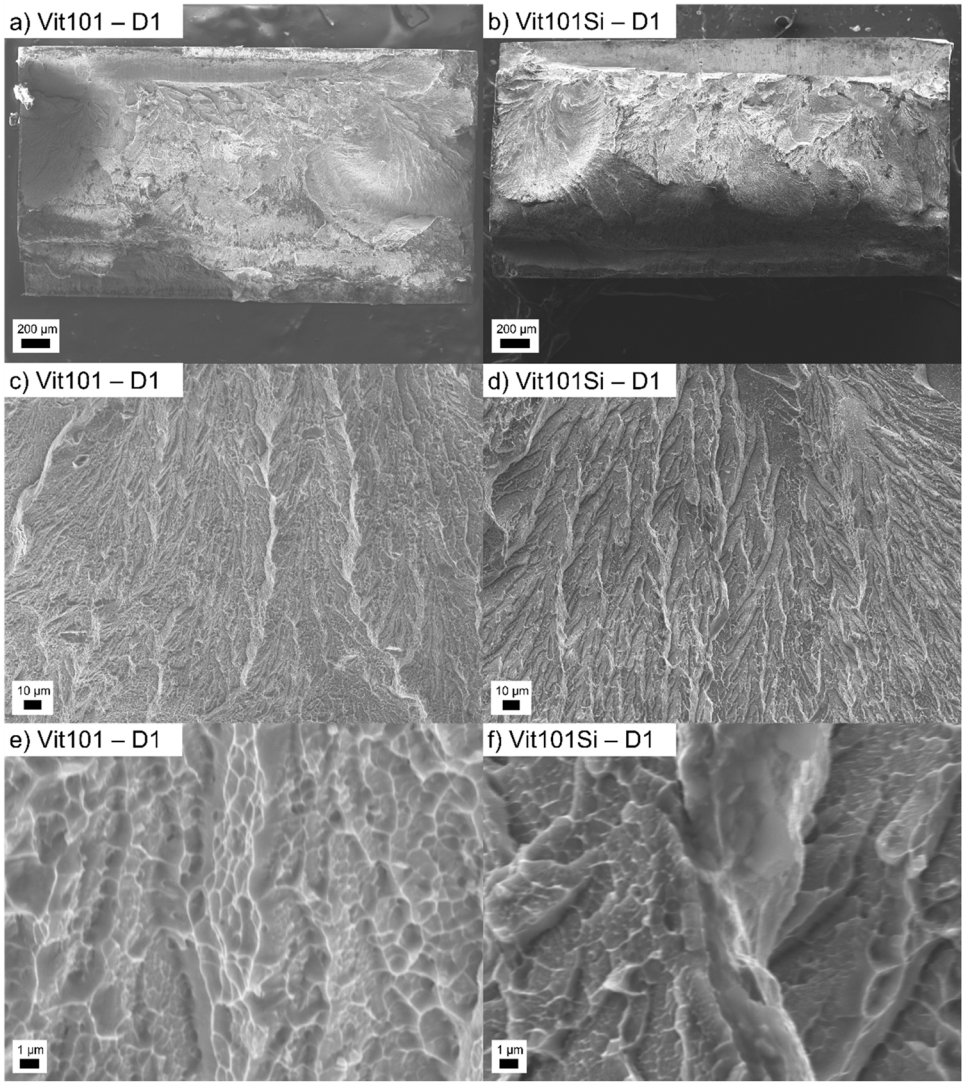

Fig. 6. SEM imaging (SE) of the fracture surfaces of tested D1 beams. (a) and (b) give an overview over the whole fracture surfaces of the Vit101 and Vit101Si samples. The beams were loaded from below, resulting in tension stress in the upper part. For both samples, a small portion on the top of the surface shows a flat appearance, most probably corresponding to the initial step of shear band forming and delamination [42]. The rest of the fracture appears rather rough, indicating a rapid fracture as a second step [42] with typical river-like pattern highlighted in (c) and (d). Zoomed-in images of the river-like structures in (e) and (f) reveal dimple pattern, which show a larger and more homogeneous structure in case of Vit101.

0.4 GPa (an increase of about 19 %) as shown in Fig. 5. The other three batches, the medium-energy C3 beams made from Vit101 as well as both Vit101Si parameter sets, show significantly lower Young's moduli and fracture strength of less than 2 GPa with large scatter among the different curves. As discussed above, crystallization can be ruled out for C3 and D1 sets as the origin of such suboptimal performance.

Regarding the results of the two Vit101 parameter sets D1 and C3 allows to directly identify the relative density as a main factor that determines the mechanical performance. The medium-energy set C3 features an 1% lower relative density than the highly densified D1 set (98.92 ± 0.61 % and 99.92 ± 0.03 %, respectively), corresponding to a higher number of remaining defects like pores or cracks. These act as stress risers and therefore lead to premature fracture before the alloy's yield strength is reached, as previously highlighted in various studies [18,49,50]. The reduced Young's modulus of the C3 set may also be explained by relative density considerations, as Shi et al. [19] have recently demonstrated that increased porosity in PBF-LB/M-formed AMZ4 leads to a decrease in Young's modulus.

The Vit101Si C3 samples also feature a suboptimal relative density (98.87 ± 0.91 %) due to the applied medium-energy parameter set. Here, the negative influence of remaining defects can be seen as origin for the diminished mechanical performance, too.

A different picture is found when comparing the D1 sets of Vit101 and Vit101Si. Both sample sets feature maximized and basically identical relative densities of 99.92 ± 0.03% and 99.87 ± 0.09 %, respectively. Accordingly, differences in relative density are ruled out as origin of the diminished performance of the Vit101Si D1 samples. Instead, the alloy-specific fracture toughness can be identified as the second main factor that determines the mechanics. Garrett et al. [25] revealed that microalloying with Si and Sn leads to embrittlement in the Vit101 system. The notch toughness K_Q of high-purity as-cast specimens was reported to decrease from 103.40 MPa $m^{1/2}$ for Vit101 to 90.92 MPa $m^{1/2}$ for Vit101Si and even 54.84 MPa $m^{1/2}$ for Vit101SiSn. Here, the circle closes towards the initially presented light microscopy results for the D1 cuboids in Fig. 1 and the cuboid overview in Figure A in the Supplementary material. Vit101Si and especially Vit101SiSn show increased crack formation, most probably since their lower toughness renders them more vulnerable to thermally induced stresses during PBF-LB/M processing. Finally, the reduced toughness leaves the Vit101Si D1 beam samples less resilient against such PBF-LB/M-typical defect sites, resulting in premature failure during the 3PBB measurements.

Xi et al. [51] have demonstrated that the size scale of viscous features like vein pattern and dimples observed in the fracture surface correlates directly with the fracture toughness of the respective BMG. Ductile BMGs tend to form homogeneous pattern with microscale sizes, while brittle systems feature smaller structures like nano-waves [42,52]. The fractograms in Fig. 6 reveal that Vit101 shows larger and more

homogeneous dimple structures in the rough rapid fracture surface region than Vit101Si, thereby well reflecting the toughness difference between the two alloys within the size scale concept introduced by Xi et al. [51].

4.4. Industrial relevance

The present evaluation process demonstrates that the non-microalloyed base alloy Vit101 is the most suitable of the three investigated systems for PBF-LB/M applications. The relatively high toughness of Vit101 allows for minimizing crack formation, resulting in superior mechanical performance, while the relatively low thermal stability plays a surprisingly neglectable role as it does not lead to unfavorable effects like thermally induced crystallization.

From an economic point of view, Vit101 ($Cu_{47}Ti_{34}Zr_{11}Ni_8$) features the advantage that it consists of relatively cheap and broadly used industry metals, mainly Cu and Ti. The small amount of the higher-priced Zr does not harshly increase the overall raw material expenses. Furthermore, it was systematically evaluated by Barreto et al. [28] that industrial-grade elemental metals can be used for successful powder atomization in just one processing step, without the need for any kind of prealloying. The present study uses exactly this industry-attractive powder produced by Barreto et al. [28] and demonstrates its applicability to additively form highly performant parts. Vit101 is therefore a possible competitor for the commercially available and already established Zr-based AMZ4 alloy. Both systems feature similar T_g, yet, as demonstrated in Fig. 5(a), additively formed Vit101 is stronger and stiffer than AMZ4. As-cast Vit101 also features a higher hardness of 576 HV5 [24] than as-cast AMZ4 with 467 HV5 [53]. Finally, AMZ4 as a Zr-based system is prone to oxygen that can, in case of high contamination levels, deteriorate the PBF-LB/M processing window as well as the mechanical performance [18]. In contrast, Vit101 has proven to be robust against oxygen contamination effects in the present study. On the other hand, the relatively high amount of Cu leaves Vit101 less resistant against corrosive attacks [31,54,55], Also, Ni might be problematic in terms of biocompatibility [31,56]. Furthermore, Vit101 still shows a certain tendency towards process-induced crack formation, while nothing comparable was reported for AMZ4 in various studies [10,13,16,18,50]. Best et al. [30] showed that as-cast AMZ4 features a K_Q of up to 138.0 MPa $m^{1/2}$, while Garrett et al. [25] reported 103.40 MPa $m^{1/2}$ for Vit101. The comparability between the notch toughness values obtained in the two different studies should be seen with caution, as K_Q depends on the tested sample dimensions and other experimental conditions, unlike the normed fracture toughness K_{IC}. Still, the difference in toughness between AMZ4 and Vit101 is also qualitatively visible in the stress-strain diagram of as-cast samples in Figure B in the Supplementary material, where AMZ4 shows distinctly higher ductility than Vit101 and the even more brittle Vit101Si. Hence, for Vit101 as the stronger, but also less tough system in the comparison, it is of special importance to minimize defect density in form of pores and cracks during PBF-LB/M processing to emphasize its superior mechanical performance.

5. Conclusion

Three CuTi-based bulk metallic glass formers, Vit101 ($Cu_{47}Ti_{34}Zr_{11}Ni_8$), Vit101Si ($Cu_{47}Ti_{33}Zr_{11}Ni_8Si_1$), and Vit101SiSn ($Cu_{47}Ti_{33}Zr_{11}Ni_6Si_1Sn_2$) were evaluated in terms of their applicability to form highly dense, amorphous, and mechanically robust PBF-LB/M parts. The Vit101 base alloy was found to be the most promising and potent alloy for PBF-LB/M processing. The addition of Si and especially Si-Sn increased thermally induced crack formation and process instability to a point that led to the exclusion of Vit101SiSn from the screening due to frequent sample loss. Vit101Si was able to form amorphous samples with low porosity over a broad parameter window, yet, the relatively low notch toughness and the tendency to form cracks prohibited optimized strength values. Vit101 showed the same robust parameter window for fully amorphous and highly dense processing but was able to reach an outstanding bending strength of about 2.5 GPa, as it features the highest toughness of the three systems.

The present work underlines that the PBF-LB/M process asks for different alloy properties than conventional casting routes to produce fully amorphous and mechanically well performing parts. GFA, conventionally defined in terms of the critical casting diameter, loses its significance in the face of a layer-wise, highly dynamic, and localized melting and vitrification process. Also, thermal stability, classically expressed via the length of the SCL region upon heating, seems to play a minor role, at least for the relatively good glass formers investigated in the present study. Instead, notch toughness and robustness against thermally induced crack formation are found as key parameters to avoid brittle products and processing issues due to structures sheared apart. Hence, future glass forming alloy development and optimization for PBF-LB/M applications should lay focus on the later aspects instead of classical casting-oriented GFA optimization.

Funding

This research was funded by the German Federal Ministry for Economic Affairs and Energy (BMWi) within the Promotion of Joint Industrial Research Program (IGF) due to a decision of the German Bundestag. It was part of the research project 21227 N (LaSaM) by the Association for Research in Precision Mechanics, Optics and Medical Technology (F.O.M.) under the auspices of the German Federation of Industrial Research Associations (AiF).

CRediT authorship contribution statement

Neuber Nico: Writing – review & editing, Methodology, Investigation, Formal analysis, Data curation. **Adam Bastian:** Writing – review & editing, Investigation, Formal analysis, Data curation. **Barreto Erika Soares:** Writing – review & editing, Project administration, Methodology, Investigation, Formal analysis, Data curation, Conceptualization. **Ruschel Lucas:** Writing – review & editing, Methodology, Investigation, Formal analysis, Data curation. **Riegler Sascha Sebastian:** Writing – review & editing, Investigation, Formal analysis, Data curation. **Jiang Hao-Ran:** Writing – review & editing, Investigation, Data curation. **Witt Gerd:** Supervision. **Kleszczynski Stefan:** Writing – review & editing, Supervision, Project administration, Funding acquisition. **Frey Maximilian:** Writing – original draft, Project administration, Methodology, Investigation, Funding acquisition, Formal analysis, Data curation, Conceptualization. **Busch Ralf:** Writing – review & editing, Supervision, Funding acquisition. **Wegner Jan:** Writing – review & editing, Project administration, Methodology, Investigation, Funding acquisition, Formal analysis, Data curation, Conceptualization. **Ellendt Nils:** Writing – review & editing, Supervision, Project administration. **Uhlenwinkel Volker:** Writing – review & editing, Supervision, Project administration, Funding acquisition.

Declaration of Competing Interest

The authors declare that they have no known competing financial interests or personal relationships that could have appeared to influence the work reported in this paper.

Data availability

Data will be made available on request.

Acknowledgments

Instrumentation and technical assistance for this work were provided by the Service Center X-ray Diffraction, with financial support from Saarland University and German Science Foundation (project number

INST 256/349–1). The authors thank Dr. Oliver Janka for the support in collection of the X-ray diffraction data presented in this paper. We want to acknowledge DESY (Hamburg, Germany), a member of the Helmholtz Association HGF, for the provision of experimental facilities. Parts of this research were carried out at PETRA III and we would like to thank Malte Blankenburg and Ulrich Lienert for assistance in using the P21.2 beamline facility.

Appendix A. Supporting information

Supplementary data associated with this article can be found in the online version at doi:10.1016/j.addma.2023.103467.

References

[1] M. Telford, The case for bulk metallic glass, Mater. Today 7 (2004) 36–43, https://doi.org/10.1016/S1369-7021(04)00124-5.
[2] U. Scipioni Bertoli, G. Guss, S. Wu, M.J. Matthews, J.M. Schoenung, In-situ characterization of laser-powder interaction and cooling rates through high-speed imaging of powder bed fusion additive manufacturing, Mater. Des. 135 (2017) 385–396, https://doi.org/10.1016/j.matdes.2017.09.044.
[3] S. Pauly, L. Löber, R. Petters, M. Stoica, S. Scudino, U. Kühn, J. Eckert, Processing metallic glasses by selective laser melting, Mater. Today 16 (2013) 37–41, https://doi.org/10.1016/j.mattod.2013.01.018.
[4] H.Y. Jung, S.J. Choi, K.G. Prashanth, M. Stoica, S. Scudino, S. Yi, U. Kühn, D. H. Kim, K.B. Kim, J. Eckert, Fabrication of Fe-based bulk metallic glass by selective laser melting: a parameter study, Mater. Des. 86 (2015) 703–708.
[5] L. Thorsson, M. Unosson, M. Teresa Pérez-Prado, X. Jin, P. Tiberto, G. Barrera, B. Adam, N. Neuber, A. Ghavimi, M. Frey, R. Busch, I. Gallino, Selective laser melting of a Fe-Si-Cr-B-C-based complex-shaped amorphous soft-magnetic electric motor rotor with record dimensions, Mater. Des. 215 (2022), 110483, https://doi.org/10.1016/j.matdes.2022.110483.
[6] X. Lu, M. Nursulton, Y. Du, W. Liao, Structural and mechanical characteristics of Cu50Zr43Al7 bulk metallic glass fabricated by selective laser melting, Materials 12 (2019), https://doi.org/10.3390/ma12050775.
[7] P. Wang, S. Pauly, L. Deng, S. Wang, P. Wang, U. Kühn, S. Pauly, Selective laser melting of a Ti-based bulk metallic glass, Mater. Lett. 212 (2017) 346–349, https://doi.org/10.1016/j.matlet.2017.10.130.
[8] X.P. Li, M.P. Roberts, S. O'Keeffe, T.B. Sercombe, Selective laser melting of Zr-based bulk metallic glasses: processing, microstructure and mechanical properties, Mater. Des. 112 (2016) 217–226, https://doi.org/10.1016/j.matdes.2016.09.071.
[9] S. Pauly, C. Schricker, S. Scudino, L. Deng, U. Kühn, Processing a glass-forming Zr-based alloy by selective laser melting, Mater. Des. 135 (2017) 133–141.
[10] J.J. Marattukalam, V. Pacheco, D. Karlsson, L. Riekehr, J. Lindwall, F. Forsberg, U. Jansson, M. Sahlberg, B. Hjörvarsson, Development of process parameters for selective laser melting of a Zr-based bulk metallic glass, Addit. Manuf. 13 (2020), 101124, https://doi.org/10.1016/j.addma.2020.101124.
[11] J. Wegner, S. Kleszczynski, S. Hechler, G. Witt, R. Busch, Parameter study about processing Zr-based bulk metallic glass with Laser beam melting, in: G. Witt (Ed.), Rapid.Tech - Int. Trade Show Conf. Addit. Manuf., Carl Hanser Verlag GmbH & Co. KG, München, 2017.
[12] J. Wegner, M. Frey, S. Kleszczynski, R. Busch, G. Witt, Influence of process gas during powder bed fusion with laser beam of Zr-based bulk metallic glasses. Proceedings of the 11th CIRP Conference on Photonic Technology, Elsevier B.V,, 2020, pp. 205–210, https://doi.org/10.1016/j.procir.2020.09.039.
[13] J. Wegner, M. Frey, P. Stiglmair, S. Kleszczynski, G. Witt, R. Busch, Mechanical properties of honeycomb structured ZR-based bulk metallic glass specimens fabricated by laser powder bed fusion, South Afr. J. Ind. Eng. 30 (3) (2019) 32–40.
[14] J. Wegner, M. Frey, R. Busch, S. Kleszczynski, Additive manufacturing of a compliant mechanism using Zr-based bulk metallic glass Chair of Manufacturing Technology, University Duisburg-Essen, 47057 Duisburg, Lotharstraße 1, Germany Chair of Metallic Materials, Saarland University, Campus C6. 3, Addit. Manuf. Lett. (2021), 100019, https://doi.org/10.1016/j.addlet.2021.100019.
[15] K. Kosiba, L. Deng, S. Scudino, Viscous flow of supercooled liquid in a Zr-based bulk metallic glass synthesized by additive manufacturing, Materials 13 (2020), https://doi.org/10.3390/MA13173803.
[16] M. Frey, J. Wegner, N. Neuber, B. Reiplinger, B. Bochtler, B. Adam, L. Ruschel, S. S. Riegler, H.-R. Jiang, S. Kleszczynski, G. Witt, R. Busch, Thermoplastic forming of additively manufactured Zr-based bulk metallic glass: a processing route for surface finishing of complex structures, Mater. Des. 198 (2021) 1–8, https://doi.org/10.1016/j.matdes.2020.109368.
[17] N. Sohrabi, J. Jhabvala, R.E. Logé, Additive manufacturing of bulk metallic glasses - process, challenges and properties: a review, Metals 11 (2021).
[18] J. Wegner, M. Frey, M. Piechotta, N. Neuber, B. Adam, S. Platt, L. Ruschel, N. Schnell, S. Sebastian, H. Jiang, G. Witt, R. Busch, S. Kleszczynski, Influence of powder characteristics on the structural and the mechanical properties of additively manufactured Zr-based bulk metallic glass, Mater. Des. 209 (2021), 109976, https://doi.org/10.1016/j.matdes.2021.109976.
[19] J. Shi, S. Ma, S. Wei, J.P. Best, M. Stolpe, B. Markert, Connecting structural defects to tensile failure in a 3D-printed fully-amorphous bulk metallic glass, Mater. Sci. Eng. A 813 (2021), 141106, https://doi.org/10.1016/j.msea.2021.141106.
[20] J.P. Best, J. Ast, B. Li, M. Stolpe, R. Busch, F. Yang, X. Li, J. Michler, J.J. Kruzic, Relating fracture toughness to micro-pillar compression response for a laser powder bed additive manufactured bulk metallic glass, Mater. Sci. Eng. A 770 (2020), 138535, https://doi.org/10.1016/j.msea.2019.138535.
[21] J. Heinrich, R. Busch, B. Nonnenmacher, Processing of a bulk metallic glass forming alloy based on industrial grade Zr, Intermetallics 25 (2012) 1–4, https://doi.org/10.1016/j.intermet.2012.02.011.
[22] V. Pacheco, D. Karlsson, J.J. Marattukalam, M. Stolpe, B. Hjörvarsson, U. Jansson, M. Sahlberg, Thermal stability and crystallization of a Zr-based metallic glass produced by suction casting and selective laser melting, J. Alloy. Compd. 825 (2020), https://doi.org/10.1016/j.jallcom.2020.153995.
[23] X.H. Lin, W.L. Johnson, Formation of Ti-Zr-Cu-Ni bulk metallic glasses, J. Appl. Phys. 78 (1995) 6514–6519, https://doi.org/10.1063/1.360537.
[24] B. Bochtler, Thermophysical and structural investigations of a CuTi- and a Zr-based bulk metallic glass, the influence of minor additions, and the relation to thermoplastic forming, 2019.
[25] G.R. Garrett, M.D. Demetriou, J. Chen, W.L. Johnson, Effect of microalloying on the toughness of metallic glasses, Appl. Phys. Lett. 101 (2012) 101–104, https://doi.org/10.1063/1.4769997.
[26] H. Choi-Yim, R. Busch, W.L. Johnson, The effect of silicon on the glass forming ability of the Cu47Ti34Zr11Ni8 bulk metallic glass forming alloy during processing of composites, J. Appl. Phys. 83 (1998) 7993–7997, https://doi.org/10.1063/1.367981.
[27] E.S. Park, H.K. Lim, W.T. Kim, D.H. Kim, The effect of Sn addition on the glass-forming ability of Cu-Ti-Zr-Ni-Si metallic glass alloys, J. Non Cryst. Solids 298 (2002) 15–22, https://doi.org/10.1016/S0022-3093(01)01047-X.
[28] E.S. Barreto, M. Frey, J. Wegner, A. Jose, N. Neuber, R. Busch, S. Kleszczynski, L. Mädler, V. Uhlenwinkel, Properties of gas-atomized Cu-Ti-based metallic glass powders for additive manufacturing, Mater. Des. 215 (2022), 110519, https://doi.org/10.1016/j.matdes.2022.110519.
[29] X. Qiu, J.W. Thompson, S.J.L. Billinge, PDFgetX2: A GUI-driven program to obtain the pair distribution function from X-ray powder diffraction data, J. Appl. Crystallogr 37 (2004) 678, https://doi.org/10.1107/S0021889804011744.
[30] J.P. Best, H.E. Ostergaard, B. Li, M. Stolpe, F. Yang, K. Nomoto, M.T. Hasib, O. Muránsky, R. Busch, X. Li, J.J. Kruzic, Fracture and fatigue behaviour of a laser additive manufactured Zr-based bulk metallic glass, Addit. Manuf. (2020), 101416, https://doi.org/10.1016/j.addma.2020.101416.
[31] A. Kuball, O. Gross, B. Bochtler, B. Adam, L. Ruschel, M. Zamanzade, R. Busch, Development and characterization of titanium-based bulk metallic glasses, J. Alloy. Compd. 790 (2019) 337–346, https://doi.org/10.1016/j.jallcom.2019.03.001.
[32] O. Gross, L. Ruschel, A. Kuball, B. Bochtler, B. Adam, R. Busch, Bulk metallic glass formation in the (Ti,Zr)-(Ni,Cu)-S system, J. Phys. Condens. Matter 32 (2020) 1–8, https://doi.org/10.1088/1361-648X/ab7c15.
[33] N. Sohrabi, J. Jhabvala, G. Kurtuldu, M. Stoica, A. Parrilli, S. Berns, E. Polatidis, S. Van Petegem, S. Hugon, A. Neels, J.F. Löf, R.E. Logé, Characterization, mechanical properties and dimensional accuracy of a Zr-based bulk metallic glass manufactured via laser powder-bed fusion, 199 (2021). https://doi.org/10.1016/j.matdes.2020.109400.
[34] Y. Li, Y. Shen, C. Chen, M.C. Leu, H.L. Tsai, Building metallic glass structures on crystalline metal substrates by laser-foil-printing additive manufacturing, J. Mater. Process. Technol. 248 (2017) 249–261, https://doi.org/10.1016/j.jmatprotec.2017.05.032.
[35] Y. Li, Y. Shen, M.C. Leu, H.L. Tsai, Mechanical properties of Zr-based bulk metallic glass parts fabricated by laser-foil-printing additive manufacturing, Mater. Sci. Eng. A 743 (2019) 404–411, https://doi.org/10.1016/j.msea.2018.11.056.
[36] P. Mercelis, J.P. Kruth, Residual stresses in selective laser sintering and selective laser melting, Rapid Prototyp. J. 12 (2006) 254–265, https://doi.org/10.1108/13552540610707013.
[37] C. Li, J.F. Liu, X.Y. Fang, Y.B. Guo, Efficient predictive model of part distortion and residual stress in selective laser melting, Addit. Manuf. 17 (2017) 157–168, https://doi.org/10.1016/j.addma.2017.08.014.
[38] A. Hussein, L. Hao, C. Yan, R. Everson, Finite element simulation of the temperature and stress fields in single layers built without-support in selective laser melting, Mater. Des. 52 (2013) 638–647, https://doi.org/10.1016/j.matdes.2013.05.070.
[39] C. Suryanarayana, A. Inoue, Bulk Metallic Glasses, CRC Press, 2011.
[40] E.S. Park, D.H. Kim, T. Ohkubo, K. Hono, Enhancement of glass forming ability and plasticity by addition of Nb in Cu-Ti-Zr-Ni-Si bulk metallic glasses, J. Non Cryst. Solids 351 (2005) 1232–1238, https://doi.org/10.1016/j.jnoncrysol.2005.02.019.
[41] M. Tang, P.C. Pistorius, J.L. Beuth, Prediction of lack-of-fusion porosity for powder bed fusion, Addit. Manuf. 14 (2017) 39–48, https://doi.org/10.1016/j.addma.2016.12.001.
[42] G.N. Yang, Y. Shao, K.F. Yao, Understanding the fracture behaviors of metallic glasses-an overview, Appl. Sci. 9 (2019), https://doi.org/10.3390/app9204277.
[43] L. Deng, K. Kosiba, R. Limbach, L. Wondraczek, U. Kühn, S. Pauly, Plastic deformation of a Zr-based bulk metallic glass fabricated by selective laser melting, J. Mater. Sci. Technol. 60 (2021) 139–146.
[44] X.H. Lin, W.L. Johnson, W.K. Rhim, Effect of oxygen impurity on crystallization of an undercooled bulk glass forming Zr–Ti–Cu–Ni–Al alloy, Mater. Trans.\ 38 (1997) 473–477, https://doi.org/10.2320/matertrans1989.38.473.
[45] D.V. Louzguine-Luzgin, C. Suryanarayana, T. Saito, Q. Zhang, N. Chen, J. Saida, A. Inoue, Unusual solidification behavior of a Zr–Cu–Ni–Al bulk glassy alloy made from low-purity Zr, Intermetallics 18 (2010) 1531–1536.
[46] A. Gebert, J. Eckert, L. Schultz, Effect of oxygen on phase formation and thermal stability of slowly cooled Zr65Al7.5Cu17.5Ni10 metallic glass, Acta Mater. 46 (1998) 5475–5482.

[47] C.T. Liu, M.F. Chisholm, M.K. Miller, Oxygen impurity and microalloying effect in a Zr-based bulk metallic glass alloy, Intermetallics 10 (2002) 1105–1112.
[48] S.C. Glade, J.F. Löffler, S. Bossuyt, W.L. Johnson, M.K. Miller, Crystallization of amorphous Cu47Ti34Zr11Ni8, J. Appl. Phys. 89 (2001) 1573–1579, https://doi.org/10.1063/1.1332089.
[49] J. Wegner, M. Frey, P. Stiglmair, S. Kleszczynski, G. Witt, R. Busch, Mechanical properties of honeycomb structured ZR-based bulk metallic glass specimens fabricated by laser powder bed Fusion, South Afr. J. Ind. Eng. 30 (2019).
[50] N. Sohrabi, A. Parrilli, J. Jhabvala, A. Neels, R.E. Logé, Tensile and impact toughness properties of a Zr-based bulk metallic glass fabricated via laser powder-bed fusion, Materials 14 (2021), https://doi.org/10.3390/ma14195627.
[51] X.K. Xi, D.Q. Zhao, M.X. Pan, W.H. Wang, Y. Wu, J.J. Lewandowski, Fracture of brittle metallic glasses: brittleness or plasticity, Phys. Rev. Lett. 94 (2005) 25–28, https://doi.org/10.1103/PhysRevLett.94.125510.
[52] C.A. Schuh, T.C. Hufnagel, U. Ramamurty, Mechanical behavior of amorphous alloys, Acta Mater. 55 (2007) 4067–4109, https://doi.org/10.1016/j.actamat.2007.01.052.
[53] B. Bochtler, M. Stolpe, B. Reiplinger, R. Busch, Consolidation of amorphous powder by thermoplastic forming and subsequent mechanical testing, Mater. Des. 140 (2018) 188–195, https://doi.org/10.1016/j.matdes.2017.11.058.
[54] C. Qin, K. Asami, T. Zhang, W. Zhang, A. Inoue, Corrosion behavior of Cu-Zr-Ti-Nb bulk glassy alloys, Mater. Trans. 44 (2003) 749–753, https://doi.org/10.2320/matertrans.44.749.
[55] H.B. Lu, L.C. Zhang, A. Gebert, L. Schultz, Pitting corrosion of Cu-Zr metallic glasses in hydrochloric acid solutions, J. Alloy. Compd. 462 (2008) 60–67, https://doi.org/10.1016/j.jallcom.2007.08.023.
[56] Y. Guo, I. Bataev, K. Georgarakis, A.M. Jorge, R.P. Nogueira, M. Pons, A.R. Yavari, Ni- and Cu-free Ti-based metallic glasses with potential biomedical application, Intermetallics 63 (2015) 86–96, https://doi.org/10.1016/j.intermet.2015.04.004.